ARTICLE OPEN

Check for updates

Bioinspired organic optoelectronic synaptic transistors based on cellulose nanopaper and natural chlorophyll-a for neuromorphic systems

Junyao Zhang[1], Dapeng Liu[1], Qianqian Shi[1], Ben Yang[1], Pu Guo[1], Lu Fang[1], Shilei Dai[1], Lize Xiong[2] and Jia Huang[1,2]✉

Inspired by human brains, optoelectronic synapses are expected as one of significant steps for constructing neuromorphic systems. In addition, intensive attention has been paid to biodegradable and biocompatible materials for developing green electronics. In this regard, environmentally friendly organic optoelectronic synaptic transistors based on wood-derived cellulose nanopaper (WCN) as dielectric/substrate and nature chlorophyll-a as photoactive material are demonstrated. Both WCN and chlorophyll-a are biocompatible and biodegradable materials from natural organisms. Versatile synaptic behaviors have been well mimicked by the modulation of both electrical and optical signals. More significantly, optical wireless communication is experimentally emulated and the information processing capability is also verified in pattern recognition simulation. Furthermore, the flexible synaptic transistors exhibit no apparent synaptic performance degradation even when the bending radius is reduced to 1 mm. Our work may develop a promising approach for the development of green and flexible electronics in neuromorphic visual systems.

npj Flexible Electronics (2022)6:30 ; https://doi.org/10.1038/s41528-022-00163-x

INTRODUCTION

Considerable attention has been attracted on neuromorphic systems based on non-Von Neumann architecture because of their potential to efficiently handle cognitive operations with low energy consumption compared with conventional computers[1–3]. A feasible stage for constructing neuromorphic systems is to explore synapse-like artificial devices. Till now, artificial synaptic devices including field-effect transistors[4–11], memristors[12–15], as well as phase change memory[16–18], have been extensively explored. Great emphasis has been put on electrical stimulation to modulate functions of artificial synaptic devices, which is suitable for the integration of an artificial neural network (ANN) with high density[19]. In recent years, motivated by the evolution of optogenetics, synaptic devices activated by optical stimulation, which benefit from the interference immunity, high bandwidth, and low power computation, are supposed as promising candidates for ultrafast neuromorphic computation[20–22]. In addition, optical-activated synaptic devices are appropriate for simulating retinal neurons, leading to building bridges between brain computing and neuromorphic visual systems[23–26]. It would be advantageous to have the synergy of electrical and optical stimulations in one single synaptic device to strengthen attainable plasticity and parallelism. More significantly, the synergy can allow the development of the robust ANN with drastically reduced devices. Thus, designing and obtaining appropriate material systems and device structures is of great significance to fabricate optoelectronic synaptic devices which can be regulated by both electrical and optical stimulations. Recently, based on diverse materials, such as perovskites[13,27], low-dimensional materials[28–31], and organic materials[32,33], a series of optoelectronic synaptic devices have been reported. These works indicate that there is a high demand and a considerable interest in designing material systems and device structures of optoelectronic synapses.

Despite rapid advancement, optoelectronic synapses based on biodegradable and biocompatible dielectrics, substrates, and photoactive materials have been barely reported. Owing to the colossal performance requirements and short lifetime of consumer electronics, electronic wastes are explosively produced and abandoned. To address this issue, the implementation of environmentally friendly optoelectronic synaptic devices is essential to the further development of green neuromorphic electronics. More strikingly, the usage of natural biomaterials makes electronic devices lightweight, cheap, flexible compared with silicon-based electronics, and renewable, biodegradable, biocompatible compared with plastic substrate-based electronics[34–37].

Here, we demonstrated environmentally friendly and flexible organic optoelectronic synaptic transistors based on wood-derived cellulose nanopaper (WCN) as both the substrate and dielectric, and organic semiconductor (OSC)/nature chlorophyll-a as the photoactive layer. Cellulose, which is one of the key components in woods, is regarded to be one of the most abundant biomaterials in the world[36]. WCNs composed of nanofibrillated cellulose (NFC) have the characteristics of outstanding mechanical properties, chemical durability, and thermal stability, and thus many green electronics have utilized WCNs as substrate materials. More significantly, benefitting from their low surface roughness and the ionic conductivity, WCNs can be simultaneously considered as potential dielectric materials, which are essential to construct high-performance optoelectronic synaptic transistors with low operating voltage. On the other hand, chlorophyll-a is also one of the most widely available natural materials, which is the main pigment for photosynthesis in plants. In addition, both polymer OSC and chlorophyll-a are excellent solution processable materials, which can be readily blended[38]. Hence, the ultrathin OSC/chlorophyll-a hybrid film could be

[1]Interdisciplinary Materials Research Center, School of Materials Science and Engineering, Frontiers Science Center for Intelligent Autonomous Systems, Tongji University, Shanghai 201804, People's Republic of China. [2]Translational Research Institute of Brain and Brain-Like Intelligence, Shanghai Fourth People's Hospital Affiliated to Tongji University, School of Materials Science and Engineering, Tongji University, Shanghai 200434, People's Republic of China. ✉email: huangjia@tongji.edu.cn

fabricated through a solution epitaxy method[39,40]. The preponderance of solution epitaxy is to eliminate the influence of dielectric surface on the morphology of the deposited hybrid film. The as-prepared optoelectronic synaptic transistors could be modulated by both optical and electrical signals at a low operating voltage of −1 V. Furthermore, typical synaptic behaviors, including short-term plasticity (STP), long-term plasticity (LTP), the conversion from STP to LTP, and spatiotemporally correlated signal processing could be simulated at the device level. More importantly, the potential of the optoelectronic synaptic transistors in optical wireless communication was experimentally investigated and the information processing was also verified in pattern recognition simulation at the system level. Additionally, the transistors exhibited no obvious synaptic performance degradation even when the bending radius was reduced to 1 mm. Finally, the environmental friendliness of the bioinspired organic optoelectronic synaptic transistors was verified through the paramecium activity test. These results may suggest a prospective path for developing next-generation green neuromorphic electronics.

RESULTS

Design of bioinspired optoelectronic synaptic transistors

Wood is extensively regarded as one kind of biocompatible and biodegradable natural material and cellulose is one of the main components in wood[36,41]. WCNs were produced from NFC pulp that was treated by (2,2,6,6-tetramethylpiperidin-1-yl)-oxidanyl (TEMPO) oxidization process (Supplementary Fig. 1a). The preparation process of WCNs is introduced in detail in the "Methods" section and Supplementary Fig. 2. Supplementary Fig. 3 displays that the as-prepared WCN exhibited high transparency. To investigate the surface morphology of the WCN, atomic force microscopy (AFM) measurement was carried out (Fig. 1a). It can be seen that TEMPO-oxidized NFCs were intertwined with each other tightly. The WCN showed an ultra-smooth surface with an average surface roughness (R_a) of 1.1 nm, which was important for constructing synaptic transistors directly on the surface of the WCN. In addition, almost no distinct pores were observed on the surface of the WCN in the scanning electron microscope (SEM) image as illustrated in an inset of Fig. 1b, which also confirmed its uniform surface flatness. Chemical structure of the WCN could be obtained using Fourier transform infrared (FTIR) spectroscopy (Fig. 1b). The peaks at 1054 and 1159 cm^{-1} were ascribed to the asymmetric stretching and bending absorption of C–O–C group. Besides, the peaks at 1313, 1406, and 1597 cm^{-1} were originated from the existence of sodium carboxylate. Other absorption peaks centered at 2901 and 3339 cm^{-1} were attributed to the stretching vibration of symmetric and asymmetric methylene and methyl C–H group, and the stretching of O–H group, respectively[41]. X-ray photoelectron spectroscopy (XPS) was utilized to further affirm the introduction of sodium ions after the TEMPO-oxidized process (Supplementary Fig. 4). The peak located at 1071 eV corresponded to the excitation of Na 1 s, and the relative content of Na element in the WCN was estimated to ~3.47% (Supplementary Table 1), which verified hydroxymethyl groups at the C6 site of glucose were partially converted into sodium carboxylate. The introduction of sodium ions contributes to the large effective capacitance of the dielectric material WCN, which enables the organic synaptic transistors to achieve low-voltage operation performance. To confirm the critical role of sodium ions, frequency-dependent capacitance of the WCN was investigated (Supplementary Fig. 5). With the decrease of frequency, the effective capacitance of the WCN increased. When the frequency was set at 20 Hz, the effective capacitance of the WCN was still as large as 215 nF cm^{-2}, which could be ascribed to the generation of the electric double layer (EDL) that mainly resulted from the movement of sodium ions in the WCN under the external electric field[8,42]. Electrochemical impedance spectroscopy was utilized to further characterize the ionic conductive characteristic of the WCN (Fig. 1c). The ionic conductivity of the WCN can be extracted from the Cole−Cole plot according to the formula:

$$\delta = \frac{d}{A(r - r_0)} \quad (1)$$

where δ, d, A, r, and r_0 represent the ionic conductivity, thickness of the WCN, electrode area, impedance real value, and electrode resistance, respectively. In our case, d was 30 μm, A was 4 mm^2, r_0 was 5 Ω, and r could be extracted from the Cole−Cole plot, which was 394 Ω. Hence, δ could be calculated as 1.93×10^{-2} S m^{-1}. This ensures that the WCN presents excellent ionic conductivity, which makes it applicable to directly build synaptic transistors on its surface. Besides, the thermal stability of the WCN was investigated (Supplementary Fig. 6). The slight decrease in weight of the WCN below 200 °C could be attributed to the loss of the adsorbed moisture. The decomposition temperature of the WCN was ~200 °C due to the rapid reduction in weight of the WCN, which was higher than the fabrication temperature of the whole device. Thus, the WCN possesses outstanding thermal stability for the preparation of most organic synaptic transistors.

Synapses are the functional links between neurons. Figure 1d shows a structural schematic diagram of a biological synapse. When action potentials are triggered, the permeability of the Ca^{2+} channel in the pre-synaptic membrane is altered, leading to the release of neurotransmitters into the synaptic cleft. Subsequently, some of the neurotransmitters interact with the receptors on the post-synaptic membrane, and then enable the information transmission. Our optoelectronic synaptic transistor is obtained to mimic the biological synapse, where either the optical stimulus exerted on the poly[2,5-bis(2-octyldodecyl)pyrrolo[3,4-c]pyrrole-1,4(2H,5H)-dione-3,6-diyl)-alt-(2,2′;5′,2″;5″,2‴-quaterthiophen-5,5‴-diyl)] (PDPP4T)/chlorophyll-a hybrid film or the electrical stimulus applied on the gate terminal is regarded as the pre-synaptic membrane, and the channel layer can be considered as the post-synaptic membrane. The synaptic transistor was fabricated by simply transferring the PDPP4T/chlorophyll-a hybrid film on the WCN through a solution epitaxy method. Supplementary Fig. 1b, c shows the molecular structures of both PDPP4T and chlorophyll-a. Figure 1e displays the photograph of the as-fabricated optoelectronic synaptic transistor array. The merit of solution epitaxy is that the ultrathin hybrid film can be directly grown onto the ultrasmooth surface of the water, which avoids the substrate effect on the growth of the thin films. AFM measurement was employed to obtain both the surface morphology and thickness of the PDPP4T/chlorophyll-a hybrid film. As depicted in Supplementary Fig. 7, the thickness of the hybrid film was ~7.9 nm and the corresponding R_a was 0.73 nm, demonstrating that an ultrathin PDPP4T/chlorophyll-a hybrid film with an ultrasmooth surface was successfully obtained. The ultrathin and ultrasmooth hybrid film endows the whole device with flexibility and bending properties. XPS measurement was employed to analyze the element composition and the distribution of chlorophyll-a in the hybrid film (Supplementary Fig. 8). The peak at 1304 eV corresponded to the excitation of Mg (1 s), which could be regarded as the characteristic element in chlorophyll-a. The contents of Mg element at different depths were almost the same, indicating the distribution of chlorophyll-a in different depths of the hybrid film was uniform and the hybrid film had no vertical phase separation. Figure 1f depicts the UV–vis absorption spectra of the PDPP4T/chlorophyll-a hybrid film, pure PDPP4T film, and pure chlorophyll-a film, respectively. Compared with the pure PDPP4T and pure chlorophyll-a films, the optical absorption of the PDPP4T/chlorophyll-a hybrid film was enhanced. An intense absorption peak of ~665 nm was observed, and thus all the light-triggered synaptic functions were emulated under the

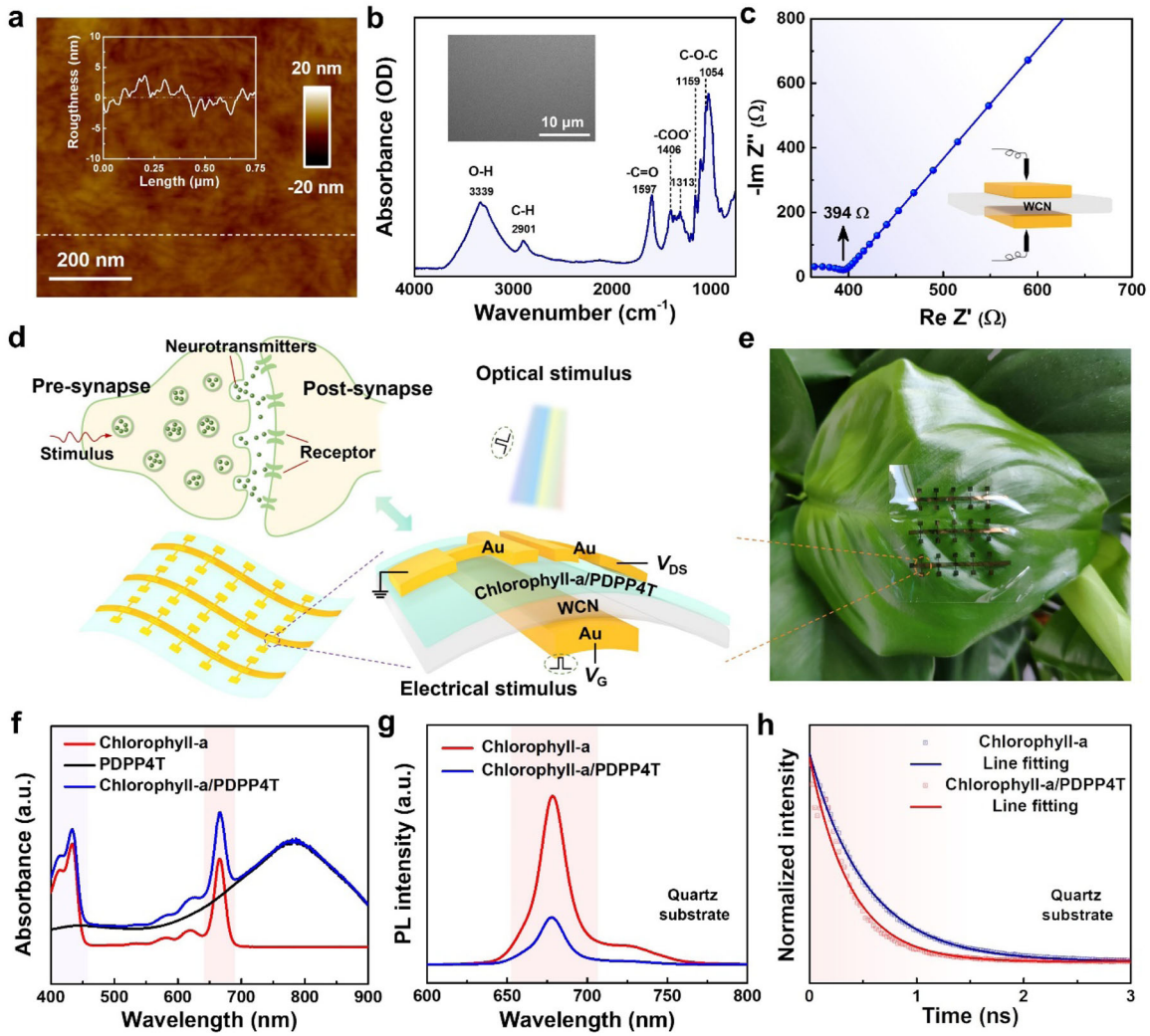

Fig. 1 Overview of bioinspired organic optoelectronic synaptic transistors. a AFM image of the WCN. The inset is the roughness curve of the WCN surface obtained from the line scan. Scale bar, 200 nm. **b** FTIR spectrum of the WCN. The inset is the top-view SEM image of the WCN. Scale bar, 10 μm. **c** Cole−Cole plot of the WCN. The inset shows the schematic diagram of device testing. **d** Schematic illustration of a biological synapse and an optoelectronic synaptic transistor. **e** A photograph of an optoelectronic synaptic transistor array. **f** UV–vis absorption spectra of the chlorophyll-a film, PDPP4T film, and PDPP4T/chlorophyll-a hybrid film, respectively. **g** Steady-state PL spectra of the chlorophyll-a film and PDPP4T/chlorophyll-a hybrid film on quartz ($\lambda_{ex} = 430$ nm). **h** Transient PL spectra of the chlorophyll-a film and PDPP4T/chlorophyll-a hybrid film on quartz ($\lambda_{ex} = 405$ nm).

665 nm light illumination. To estimate the charge-transfer efficiency between PDPP4T and chlorophyll-a, steady-state photoluminescence (PL) measurement was performed on the PDPP4T/chlorophyll-a hybrid film and pure chlorophyll-a film (Fig. 1g). Obviously, the PL of the PDPP4T/chlorophyll-a hybrid film was quenched compared with the PL of the pure chlorophyll-a film, suggesting that the recombination rate of photo-generated holes and photo-generated electrons was reduced. The effective separation of the photo-generated excitons in the PDPP4T/chlorophyll-a hybrid film is important to high-performance optoelectronic devices. Moreover, PL decay kinetics for the PDPP4T/chlorophyll-a hybrid film and pure chlorophyll-a film could further reveal the process of charge transfer (Fig. 1h). Double-exponential function could be used to fit the PL decay kinetics to extract the corresponding fluorescent lifetime parameters. The value of the fast component of fluorescent lifetime was 0.53 ns for the pure chlorophyll-a film, which was larger than that for the PDPP4T/chlorophyll-a hybrid film (0.38 ns). The existence of PDPP4T promotes the fast exciton separation at the interface with the chlorophyll-a, which results in a short lifetime of excitons[43,44]. This also suggests the efficient charge transfer to the increase of photoresponse in the synaptic transistors based on the PDPP4T/chlorophyll-a hybrid film.

Simulation of typical synaptic behaviors

Basic transfer characteristic curve of the optoelectronic synaptic transistor was investigated (Supplementary Fig. 9a). The operating voltage was below −5 V, and an obvious clockwise hysteresis window was observed owing to the movement of positive ions in the WCN. Besides, the output characteristic curves of the optoelectronic synaptic transistor were also investigated (Supplementary Fig. 9b). Biologically, synaptic weight refers to the strength of the connection between pre-synapses and post-synapses, which can be regulated by action potentials[44,45]. When potential pulses act on pre-synapses, neurotransmitters are released, bringing about the changes of post-synaptic currents. The release of excitatory neurotransmitters results in the excitatory post-synaptic current (EPSC), leading to the strengthening of synaptic weight. A typical EPSC behavior triggered by an electrical spike with a negative V_G of −2 V was simulated in our

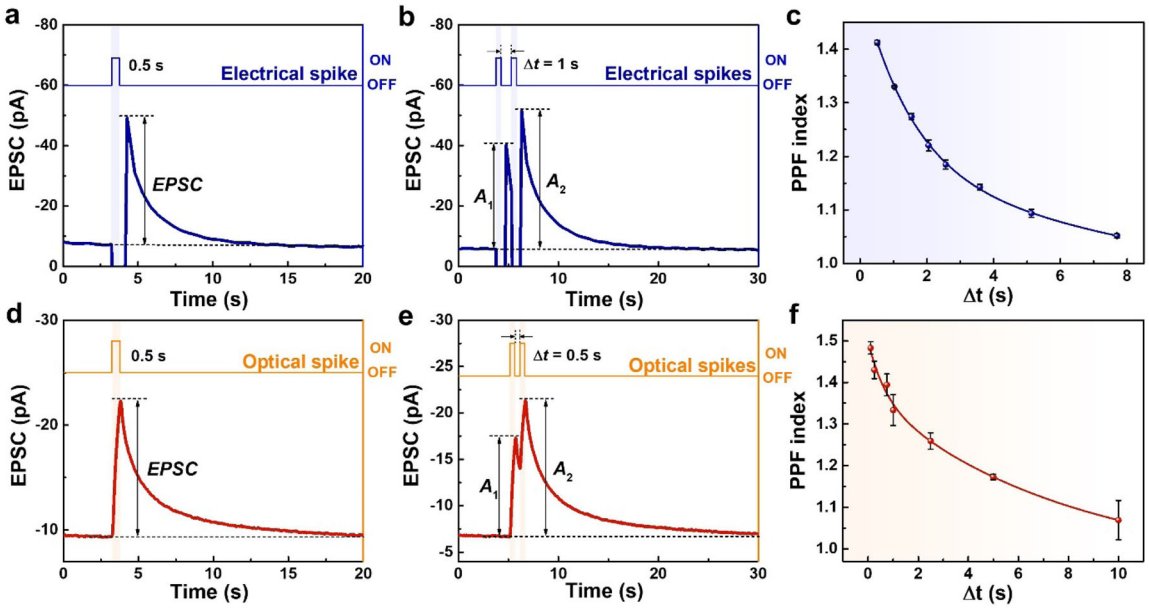

Fig. 2 Typical synaptic behaviors mimicked by the optoelectronic synaptic transistor. a EPSC evoked by an electrical spike (−2 V, 0.5 s). **b** EPSC evoked by a pair of successive electrical spikes (−2 V, 0.5 s) with an interval time of 1 s. **c** PPF index as a function of electrical spike interval with a fixed gate voltage of −2 V and a spike duration of 0.5 s. The blue solid curve is fitting with an exponential function. Error bars represent standard errors of the optoelectronic synaptic transistor investigated by three independent measurements. **d** EPSC evoked by an optical spike (665 nm, 0.50 mW cm^{-2}, 0.5 s). **e** EPSC evoked by a pair of successive optical spikes (665 nm, 0.14 mW cm^{-2}, 0.5 s) with an interval time of 0.5 s. **f** PPF index as a function of optical spike interval with fixed optical spike parameters (665 nm, 0.14 mW cm^{-2}, 0.5 s). The red solid curve is fitting with an exponential function. Error bars represent standard errors of the optoelectronic synaptic transistor investigated by three independent measurements. All the measurements of synaptic characteristics are performed at $V_D = -1$ V.

optoelectronic synaptic transistor (Fig. 2a). At the end of the electrical spike, the EPSC achieved the maximum value of ~−49 pA, followed by a gradual recover to the initial state. Such a behavior quite resembles that observed in a biological synapse[46]. The electrically-stimulated EPSC in the synaptic transistor is mainly attributed to the movement of ions in the WCN dielectric (Supplementary Fig. 10a)[8,42]. Owing to the entanglement of high rigid cellulose main chains, the anion groups on the main chains can hardly move[36]. Only several small positive irons existing in the WCN, such as sodium ions, are moveable when an electric field is applied. Therefore, a negative electrical spike gives rise to the migration of positive irons to the gate terminal, which causes net negative ions accumulating near the PDPP4T/WCN interface. An increase of carriers triggered by the accumulation of the net negative ions near the PDPP4T/WCN interface through electrostatic coupling effect contributes to the increase of the channel charge carriers, which indeed causes the increase of the channel current. Once the negative electrical spike is removed, the positive ions accumulated around the gate terminal will continuously diffuse back to the equilibrium condition because of the concentration gradient. Correspondingly, the density of channel charge carriers will gradually decrease to its initial state, which results in the decrease of the channel current, leading to the EPSC behavior. Paired-pulse facilitation (PPF) as one typical STP behavior, refers to an enhanced post-synaptic response, which can be obtained by applying a pair of successive spikes[46,47]. Figure 2b demonstrates the PPF characteristic emulated by two identical successive electrical spikes. It is observed that the amplitude of EPSC evoked by the second spike was larger than that evoked by the first one. To further investigate the PPF characteristic of our synaptic transistor, the PPF index is introduced as $A_2/A_1 \times 100\%$, where A_1 and A_2 represent the amplitude of EPSC evoked by the first and the second spike, respectively. Figure 2c plots the dependence of the PPF index evoked by electrical spikes on the time interval (Δt) between two successive electrical spikes. A maximum PPF index of 142% was achieved and the PPF index decreased exponentially with the increase of Δt.

Meanwhile, the EPSC behavior could also be triggered by an optical spike in our synaptic transistor (Fig. 2d). Similarly, EPSC evoked at the end of the optical spike achieved the maximum value of ~−22 pA, followed by a gradual recover to the original state. Under the light illumination, the photo-generated electrons can be trapped at both chlorophyll-a and PDPP4T/chlorophyll-a interfaces, while photo-generated holes can be transferred from chlorophyll-a to PDPP4T, resulting in a photocurrent (Supplementary Fig. 10b). The effective separation of the photo-generated excitons is also consistent with the PL results. After the removal of light illumination, the electrons trapped will have a slow releasing behavior and a recombination process with the holes, which lead to a delayed decay effect of the EPSC behavior[31,48–51]. To verify this mechanism, the synaptic transistor based on the pure PDPP4T film deposited on the WCN was presented (Supplementary Fig. 11). Compared with the synaptic transistor based on the PDPP4T/chlorophyll-a hybrid film, the synaptic transistor based on the pure PDPP4T film presented a lower photoresponse and a much weaker delayed decay effect. The weak delayed decay effect can be attributed to the polar groups on the surface of the WCN, which caused the photo-generated electrons to be trapped at the PDPP4T/WCN interfaces. Moreover, it should be noted that the PDPP4T film itself cannot bring about the delayed decay effect of the EPSC (Supplementary Fig. 12). The PPF behavior was also obtained by two identical successive optical spikes (Fig. 2e). Since the holes evoked by the first spike could not be released in a short time, the amplitude of EPSC evoked by the second spike was enhanced, resulting in an increased channel current. The dependence of the PPF index evoked by optical spikes on Δt is demonstrated in Fig. 2f. Similarly, the PPF index significantly increased as Δt reduced.

In human brains, STP refers to a temporary change in synaptic weight, which only lasts for a short time, while LTP can last from minutes to years[46,52]. The level of memory stored in the brain

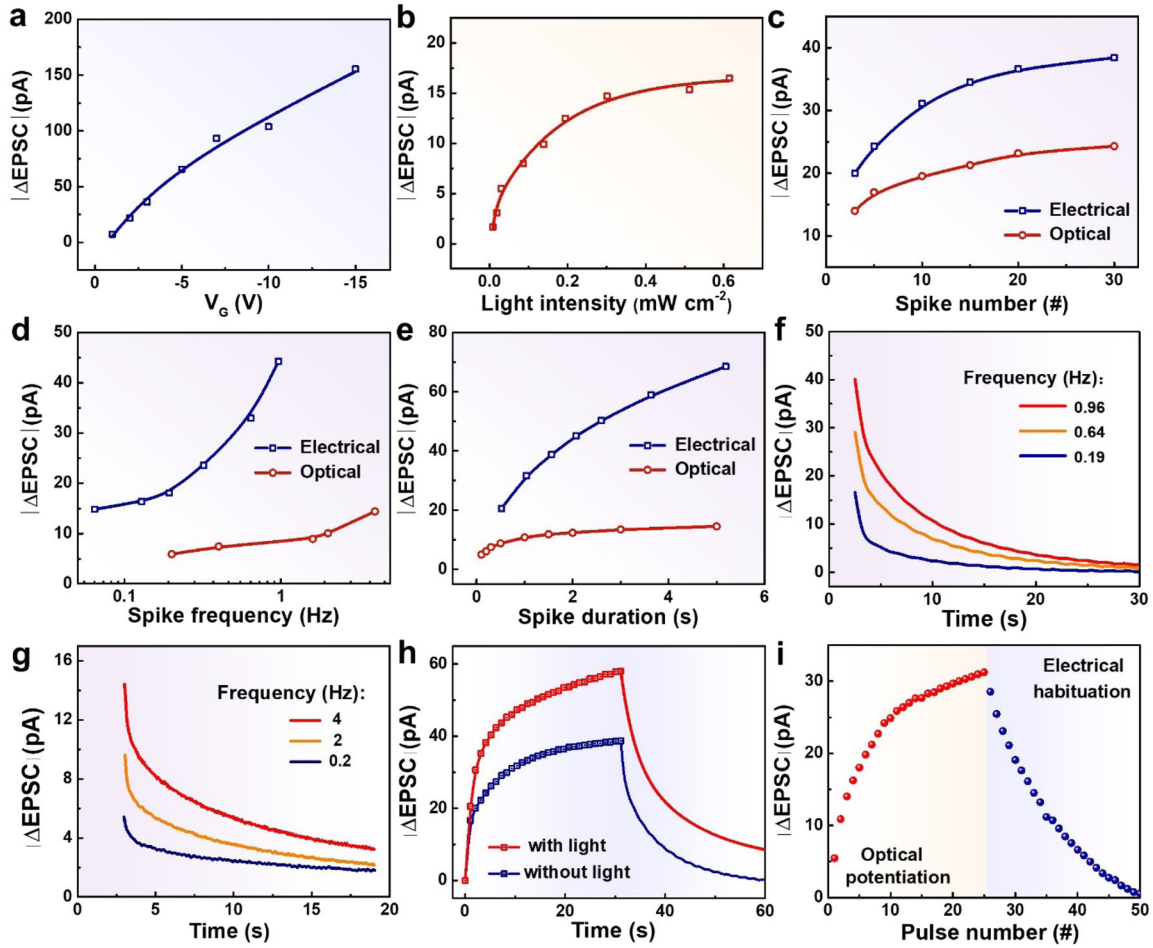

Fig. 3 Output characteristics of the optoelectronic synaptic transistor. a EPSC behaviors regulated by electrical spikes with different intensities of V_G (0.5 s). **b** EPSC behaviors regulated by optical spikes with different light intensities (665 nm, 0.5 s). **c** EPSC behaviors regulated by electrical or optical spikes with different numbers (electrical spike: −2 V, 0.5 s, 1 Hz; optical spike: 665 nm, 0.20 mW cm^{-2}, 0.5 s, 1.43 Hz). **d** EPSC behaviors regulated by electrical or optical spikes with different frequencies (electrical spike: −2 V, 0.5 s; optical spike: 665 nm, 0.20 mW cm^{-2}, 0.2 s). **e** EPSC behaviors regulated by electrical or optical spikes with different durations (electrical spike: −2 V; optical spike: 665 nm, 0.20 mW cm^{-2}). Memory decay processes after the training sequences with different frequencies under **f** electrical and **g** optical stimulations (electrical spike: −2 V, 0.5 s; optical spike: 665 nm, 0.20 mW cm^{-2}, 0.2 s). **h** Learning and memory behaviors induced by 30 electrical spikes (−2 V, 0.5 s) with and without light illumination (665 nm, 0.20 mW cm^{-2}), respectively. **i** Optical potentiation and electrical habituation characteristics subjected to a series of optical spikes (665 nm, 0.03 mW cm^{-2}, 1 s) and electrical spikes (−0.5 V, 0.6 s) under the gate voltage of −0.6 V.

usually relies on the frequency of memory and the intensity of learning. Figure 3a indicates the change values of EPSCs (ΔEPSCs) triggered by electrical spikes with different intensities of V_G in the synaptic transistors. It can be seen that a stronger electrical spike induced a higher ΔEPSC. Similar behaviors were also simulated by optical spikes with different light intensities (Fig. 3b). ΔEPSC increased quickly when the light intensity was relatively low, and then tended to saturation. In addition, the synaptic plasticity of the synaptic transistors could also be regulated by tuning spike number, spike frequency, as well as spike duration under both electrical and optical stimulations (Fig. 3c–e). With the increase of spike number, frequency, or duration, ΔEPSC was gradually enhancing from weak to strong. This phenomenon agrees well with the conversion from STP to LTP in human brains. To further investigate the memorizing behavior in our synaptic transistor, the memory decay processes after the training sequences under both electrical and optical stimulations were demonstrated in Fig. 3f, g. It is obvious that ΔEPSC decayed rapidly in the beginning stage followed by a gradually slow decay process, and a higher spike frequency led to a more remarkable ΔEPSC response and a longer memory retention, which was also similar to the conversion from STP to LTP in biological systems.

In general, humans have better learning and memory abilities under a tense situation than under a normal condition. Our synaptic devices have been demonstrated to mimic this interesting stressful learning and memory behaviors (Fig. 3h). Herein, the light signal acted as the stress element from the external environment. ΔEPSC induced by 30 electrical spikes was measured with and without light illumination, respectively. Under the application of electrical spikes, the increase of ΔEPSC in all regions with light illumination was larger than that without light illumination. Furthermore, for each spike, ΔEPSC with light assisting also increased more significantly than that without light assisting. In addition, similar trend was found in the decay process. ΔEPSC triggered by the electrical spikes with light illumination in the decay process was still larger than that triggered without light illumination, and the corresponding ΔEPSC decayed more slowly, resulting in a longer memory retention of the synaptic device. These phenomena resemble the learning and memory behaviors under stress in humans. The synaptic potentiation plasticity and habituation plasticity were further investigated under the

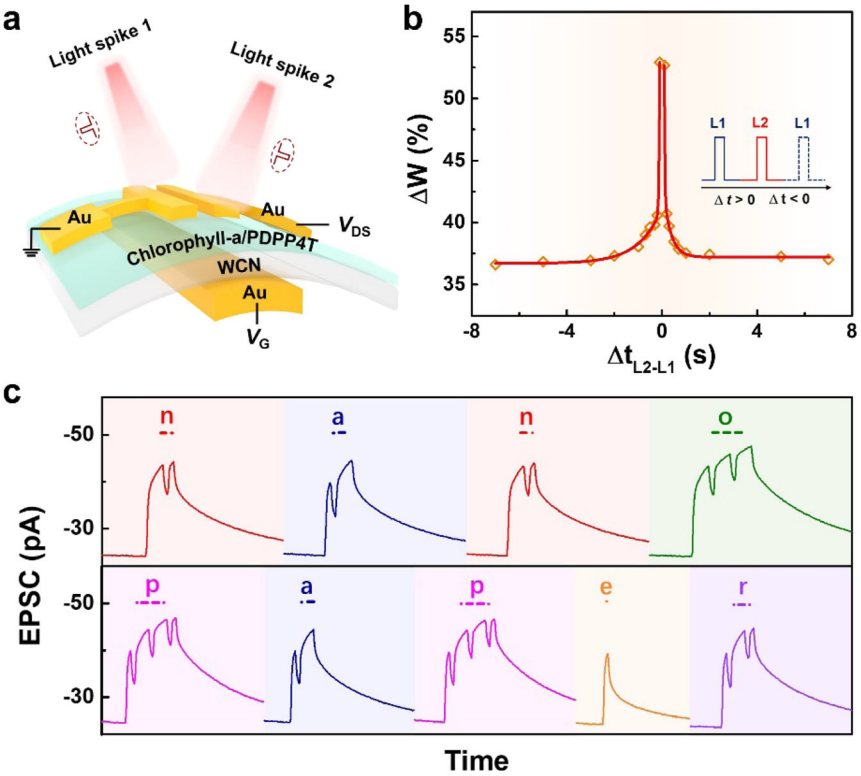

Fig. 4 Demonstrations of spatiotemporal summation and optical wireless communication. a Schematic of the simulating of spatiotemporal summation in the optoelectronic synaptic transistor by employing two optical spikes with the Δt_{L2-L1} (665 nm, 0.20 mW cm^{-2}, 0.2 s). **b** ΔW as a function of Δt_{L2-L1}. **c** EPSCs evoked by a series of optical spikes (665 nm, 0.20 mW cm^{-2}) with the International Morse code of 'NANOPAPER'. The spike duration of dot and dash patterns are 0.5 and 1.5 s, respectively, and the interval between two optical spikes is fixed at 0.5 s.

synergism of both optical and electrical stimulations. Figure 3i demonstrates the optical potentiation and electrical habituation characteristics in the optoelectronic synaptic transistor. ΔEPSC increased stepwise by applying 25 optical training spikes in the first stage, which corresponded to the synaptic potentiation plasticity. While under the next electrical training spikes, positive ions in the WCN dielectric were driven to the PDPP4T/WCN interface because of the relatively positive voltage compared with the gate voltage. Thus, the charge carriers in the channel layer decreased gradually and the ΔEPSC reduced stepwise, corresponding to the synaptic habituation plasticity.

In a natural network, spatiotemporally correlated spikes from multiple neurons can be utilized to evoke a post-synaptic current through the synapses of the post-synaptic neuron to trigger a dynamic logic[42,53]. The basic dynamic logic was demonstrated in a multi-neural system based on our synaptic transistor by employing two optical spikes with an inter-spikes time interval (Δt_{L2-L1}) as two pre-synapses (Fig. 4a). The EPSC evoked by the first spike will be superimposed on the EPSC evoked by the second spike, leading to an increase of the final EPSC. The synaptic weight change (ΔW) can be utilized to estimate the strength of spatiotemporal summation, which is introduced as $(EPSC_2 - EPSC_1)/EPSC_1 \times 100\%$, where $EPSC_1$ and $EPSC_2$ denote the EPSC peak value evoked by the first and the second spike, respectively. ΔW is deemed to depend on Δt_{L2-L1}, and hence the ΔW as a function of Δt_{L2-L1} is illustrated in Fig. 4b. When spike 1 and spike 2 were applied simultaneously ($\Delta t_{L2-L1} = 0$), a maximum superimposition ΔW of 53% in the post-synapse was achieved. As $|\Delta t_{L2-L1}|$ increased, the superimposition ΔW reduced symmetrically. This simulation of spatiotemporally correlated signal processing is of great significance for neuromorphic computing system. To further investigate the potential of our optoelectronic synapse in optical wireless communication, the International Morse codes were used as patterned optical signals. As shown in Fig. 4c, Supplementary Fig. 13, and Supplementary Fig. 14, the synaptic device could accurately react to the test letters in the English alphabet, and demonstrate a reliable EPSC response for every letter, which suggests the synaptic transistor possesses outstanding STP performance and has a potential in the application of optical wireless communication.

Demonstration of pattern recognition simulation

On the basis of tunable conductance in the synaptic transistor, a single-layer perceptron (SLP)-based ANN is simulated for supervised learning assignment with the Modified National Institute of Standards and Technology (MNIST) handwriting image database. The proposed ANN is composed of 785 input neurons and 10 output neurons with full connection by 7850 synaptic weights (Fig. 5a). Each input vector (V_i) is paired with an input neuron, which can receive input from a pixel of a binarized MNIST image. Input vector (V) is multiplied by synaptic weight matrix (W), and then the achieved current vector (I) can be converted by the sigmoid activation function to obtain output value ($y = f(I)$). Based on a weight updating method with a backpropagation (BP) algorithm, synaptic weights in the SLP-based ANN can be calculated and updated using the difference between the output values (y) and the label values[43,54]. In this case, the simulation result of '0' was taken as an example and the output signals for '0–9' numbers during the training process of 1100 phases are shown in Fig. 5b. With the increase of training phase, the output of '0' was obviously higher than that of the other numbers, indicating that '0' could be successfully recognized. The recognition rates of each number from '0 to 9' were summarized to investigate the performance of the ANN quantitatively, which showed distinct recognition rates for different numbers (Fig. 5c). The overall recognition accuracy could achieve ~79% after the ANN training

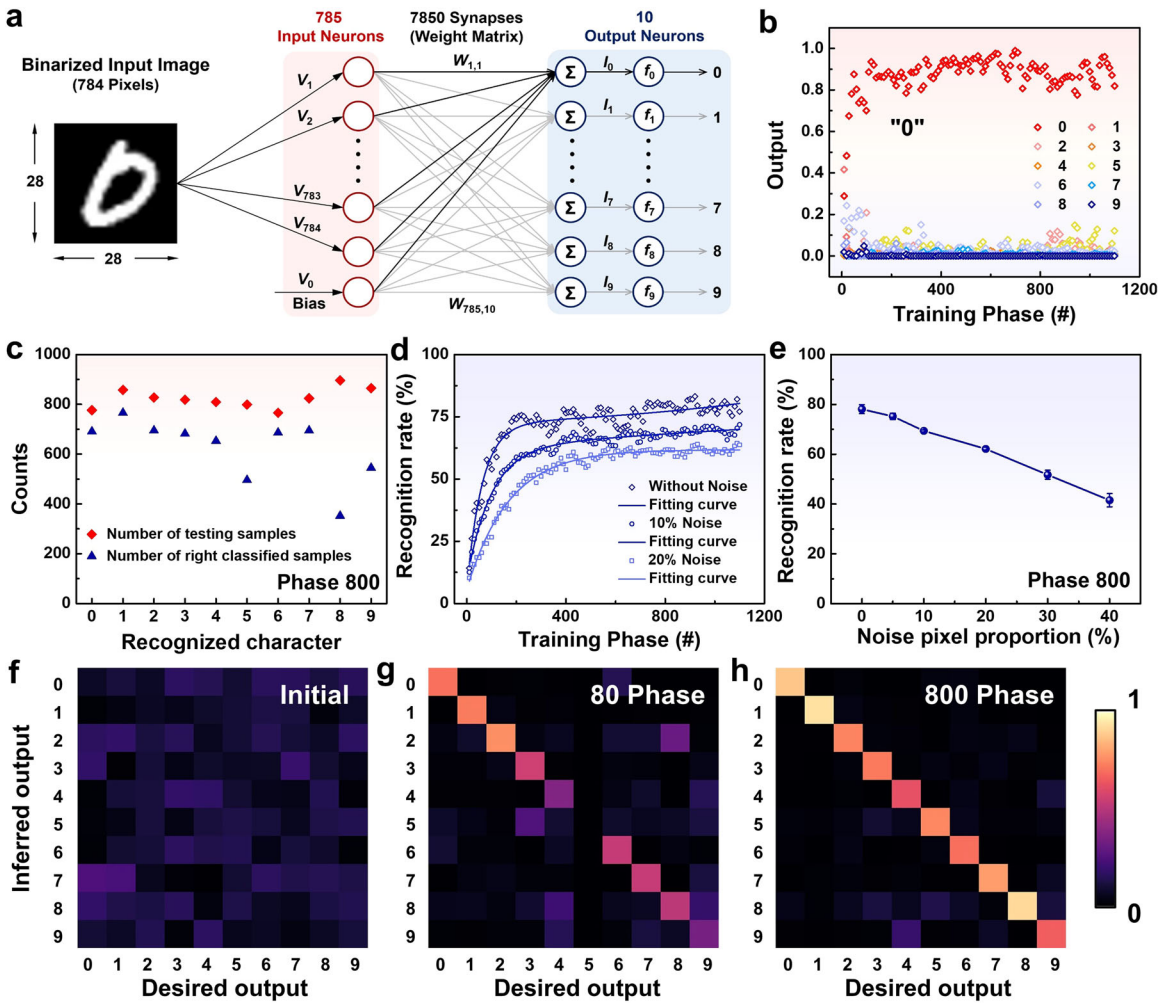

Fig. 5 A demonstration of pattern recognition simulation. a Schematic of the SLP-based ANN consisting of 785 input neurons and 10 output neurons. **b** Output signals of 10 numbers as a function of training phase. The number '0' can be recognized from other numbers because of the maximum output. **c** Recognition accuracy of 10 numbers from '0' to '9' at the 800th phase. **d** Recognition rate as the function of training phase under different noise pixel proportion (0, 10%, and 20%). **e** Recognition rate as the function of noise pixel proportion (0 −40%). Error bars represent standard errors investigated by three times independent pattern recognition processes. **f** Confusion matrix of recognition results before training. Confusion matrices of recognition results at **g** the 80th phase and **h** the 800th phase. When a large value appears on the diagonal line, the corresponding number can be successfully identified.

of 800 phase utilizing the MNIST images without noise, and the ANN also presented outstanding fault-tolerant capability (Fig. 5d, e and Supplementary Fig. 15). The overall recognition accuracy of ~50% could still be obtained even when the noise level was set at 30%. To further visualize the training process of supervised learning, the colors of diagonal in confusion matrix were used to represent the progressive learning process in the ANN (Fig. 5f–h). As the training phase increased, the maximum inferred output value of each row gradually conformed to the desired output value of each column, suggesting all numbers from '0 to 9' could be well identified.

Flexibility and biological toxicity tests

To examine the flexibility of our optoelectronic synaptic transistors, the synaptic performance of the devices at the bending state was investigated (Fig. 6a, b). To compare the test results intuitively, the EPSC induced at the bending condition was normalized to that induced at the flat condition. The EPSCs were emulated without obvious degradation at the bending states with the radius even decreased to 1 mm, which confirmed the feasibility of our devices for the application of flexible and wearable electronics.

Currently, most optoelectronic synaptic devices have been composed by non-biocompatible or even toxic materials, which inevitably cause critical ecological challenges. Thus, green electronics, which are friendly to the environment, have been paid more and more attention. Here, both WCN and chlorophyll-a are natural biocompatible materials in the optoelectronic synaptic transistors. To confirm the environmental friendliness of the devices, the biological toxicity test was conducted. Paramecium, as one kind of familiar single-celled organism, is extremely susceptible to the external environment[35]. Therefore, the as-fabricated synaptic transistors were placed in the paramecium culture medium to explore the effect on the paramecium activity (Fig. 6c, d). In order to ensure the reliability of the biological toxicity test, another paramecium culture medium was set as the control group. The 3D optical microscope was utilized to achieve the intuitive observation of the active movement of paramecia. Filaments were employed to reduce the speed of paramecium movement for precise observation. As a result, after cultured for 5 days under the same suitable conditions, the paramecia in the device group and the control group both showed obvious activity,

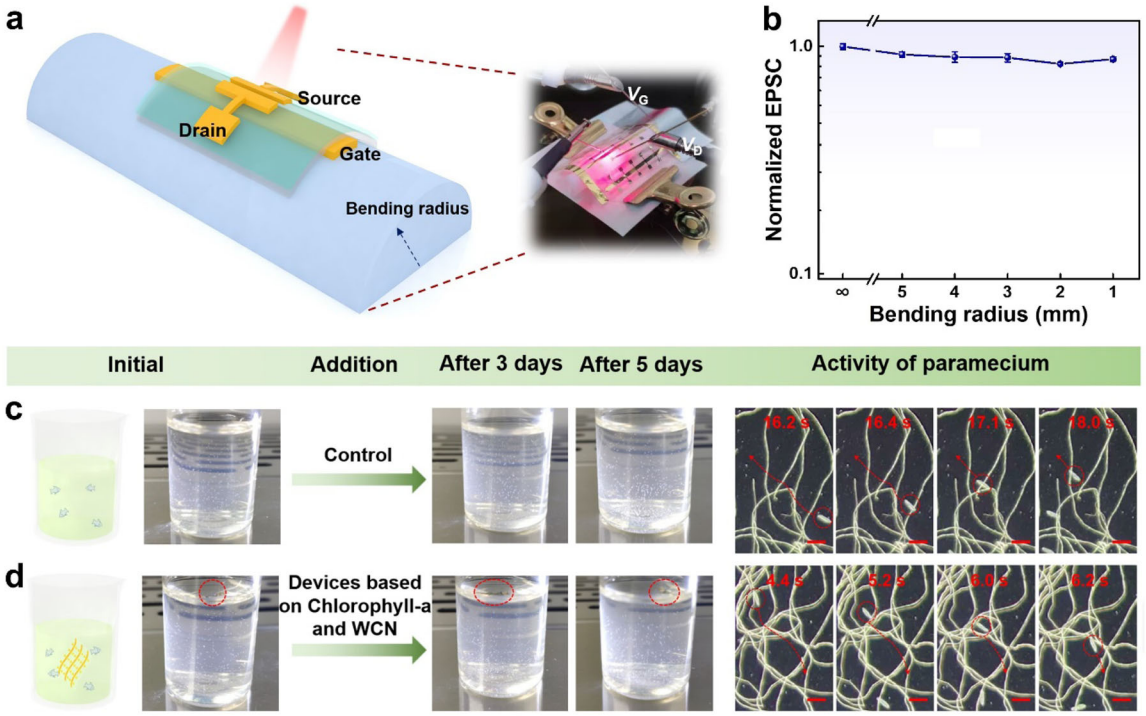

Fig. 6 Flexibility tests and biological toxicity tests of the optoelectronic synaptic transistor. a Schematic and photograph of bending tests on optoelectronic synaptic transistors. **b** Normalized EPSC (normalized to the initial EPSC tested under the flat condition) as a function of bending radius. Error bars represent standard errors investigated by three times independent measurements of the synaptic transistor. Biological toxicity tests based on **c** a pure paramecium culture medium and **d** a paramecium culture medium with an optoelectronic synaptic transistor array. The red arrows in the 3D optical microscopic images illustrate the trajectory of paramecia. The scale bar in the 3D optical microscopic images is set as 200 μm.

which suggested the paramecia were still alive. Even after 10 days of cultivation, quite a few paramecia were still alive (Supplementary Fig. 16). More importantly, both WCN and chlorophyll-a are also biodegradable, which can return back to the ecosystem after degrading by microorganisms and avoid the recycling cost of waste electronic equipment. These results indicate our optoelectronic synaptic transistors are environmentally friendly and have a wide potential for future eco-friendly electronics.

DISCUSSION

In summary, we have demonstrated environmentally friendly organic optoelectronic synaptic transistors based on WCN as dielectric/substrate and nature chlorophyll-a as photoactive material. A solution epitaxy method is utilized to fabricate the optoelectronic synaptic transistors. The synaptic devices can be regulated by both optical and electrical signals. A series of typical synaptic behaviors including EPSC, PPF, the conversion from STP to LTP, and spatiotemporally correlated signal processing have been well simulated. Furthermore, owing to the outstanding tunability between STP and LTP of the optoelectronic synaptic transistor, both the optical wireless communication is experimentally mimicked and the information processing capability can be verified by pattern recognition simulation. Moreover, our synaptic transistors exhibited no distinct synaptic performance degradation even when the bending radius was decreased to 1 mm. This work may provide a promising guide for the advancement of neuromorphic electronics based on natural biomaterials.

METHODS

Materials

PDPP4T (Poly[2,5-bis(2-octyldodecyl)pyrrolo[3,4-c]pyrrole-1,4(2H,5H)-dione-3,6-diyl)-alt-(2,2′;5′,2″;5″,2‴-quaterthiophen-5,5‴-diyl)]) and chlorophyl-a were obtained from Ossila Co., Ltd. and FUJIFILM Wako Pure Chemical Corporation without further purification, respectively. Sodium hypochlorite (NaClO), (2,2,6,6-tetramethylpiperidin-1-yl)-oxidanyl (TEMPO), and (tridecafluoro-1,1,2,2-teterahydrooctyl)-trichlorosilane (FOTS) were purchased from Aladdin, Sigma-Aldrich, and Suna Tech Inc., respectively.

Fabrication of WCNs

7.0 g of softwood pulp was suspended in 75 mL deionized water with violent agitation. 140 mg TEMPO was ultrasonically treated in 130 mL deionized water to achieve homogeneous solution. 850 mg of Sodium bromide (NaBr) was dissolved in 85 mL of deionized water, and then blended with TEMPO homogeneous solution. Afterward, the blended NaBr/TEMPO and the additional 50 mL of NaClO aqueous solution (12%) were mixed into the softwood pulp suspension. 0.5 M sodium hydroxide (NaOH) solution was added into the blended suspension so as to maintain the pH value at 10.5 for 3.5 h. Then, the product was purified by washing with deionized water for three times, followed by diluting with deionized water and dispersing to nanofibers in a crusher. After the high-speed centrifugation at 8000 rpm for 15 min, the nanofibers were separated from the microfibers and the supernatant was collected. Furthermore, ultimate cellulose nanofiber pulp was poured into the culture dishes pretreated by FOTS, and then dried naturally. Finally, WCNs were prepared which were easy to be stripped off from the culture dish.

Fabrication of the ultrathin PDPP4T/chlorophyll-a hybrid film

15 μL of the pre-prepared organic semiconductor PDPP4T/chlorophyll-a solution (0.5 mg chlorophyll-a and 5 mg PDPP4T dissolved in 1 mL mixed solvent of chloroform and chlorobenzene) was dropped in a petri dish which was equipped with ultrapure water. A few hours later, a WCN was placed on the PDPP4T/chlorophyll-a hybrid film which grew completely.

Through the tension of water, the hybrid film was pressed to the surface of the WCN and closely adhered to the WCN. After that, the WCN with the hybrid film was dried for 2 h in a vacuum environment. Finally, 40 nm Au source–drain and gate electrodes were thermally evaporated on the top of the PDPP4T/chlorophyll-a hybrid film and the back of the WCN through shadow masks. The channel width/length ratio was 20.

Characterization

A UV–vis spectrometer (Agilent Technologies Co., Ltd., Cary 60) and a spectrophotometer (Hitachi, F-7000) were used to record the UV–vis absorption spectra and steady-state PL spectra, respectively. A XperRam 200 was employed to obtain PL decay dynamics. AFM (Bruker Inc.) was employed to obtain surface morphologies of the WCN and the PDPP4T/chlorophyll-a hybrid film, and to measure the thickness of the PDPP4T/chlorophyll-a hybrid film. SEM (Nova Nano SEM 450) was used to observe the surface morphology of the WCN. FTIR spectroscopy (EQUINOX 55) was used to characterize the chemical structure of the WCN. XPS (ESCALAB 250Xi) was employed to analyze the distribution of chlorophyll-a in the hybrid films. Effective capacitance and ionic conductivity of the WCN were investigated by a LCR meter (Tonghui TH2827C) and electrochemical station (Bio-logic SAS, VMP-3), respectively.

All electrical properties of synaptic transistors were measured by the Keithley 4200 and PDA Fs-Pro semiconductor characterization system in vacuum. Grating monochromators (Omno 330150, Beijing NBeT) and Xenon lamps were used to provide light sources of different wavelengths and intensities.

DATA AVAILABILITY

The data that support the findings of this study are available from the corresponding author upon reasonable request.

CODE AVAILABILITY

Code from this study is available from the corresponding author upon reasonable request.

Received: 18 November 2021; Accepted: 30 March 2022;
Published online: 24 May 2022

REFERENCES

1. Tang, J. et al. Bridging biological and artificial neural networks with emerging neuromorphic devices: Fundamentals, progress, and challenges. *Adv. Mater.* **31**, e1902761 (2019).
2. van de Burgt, Y., Melianas, A., Keene, S. T., Malliaras, G. & Salleo, A. Organic electronics for neuromorphic computing. *Nat. Electron.* **1**, 386–397 (2018).
3. Chai, Y. In-sensor computing for machine vision. *Nature* **579**, 32–33 (2020).
4. Han, H., Yu, H., Wei, H., Gong, J. & Xu, W. Recent progress in three-terminal artificial synapses: From device to system. *Small* **15**, e1900695 (2019).
5. Cho, S. W., Kwon, S. M., Kim, Y.-H. & Park, S. K. Recent progress in transistor-based optoelectronic synapses: From neuromorphic computing to artificial sensory system. *Adv. Intell. Syst.* **3**, 2000162 (2021).
6. Ling, H. F. et al. Electrolyte-gated transistors for synaptic electronics, neuromorphic computing, and adaptable biointerfacing. *Appl. Phys. Rev.* **7**, 011307 (2020).
7. Pan, X., Zheng, Y., Shi, Y. & Chen, W. Surface charge transfer doping enabled large hysteresis in van der Waals heterostructures for artificial synapse. *ACS Mater. Lett.* **3**, 235–242 (2021).
8. He, Y. et al. Spatiotemporal information processing emulated by multiterminal neuro-transistor networks. *Adv. Mater.* **31**, e1900903 (2019).
9. Zhang, S. et al. Selective release of different neurotransmitters emulated by a p-i-n junction synaptic transistor for environment-responsive action control. *Adv. Mater.* **33**, e2007350 (2021).
10. Lee, Y. et al. Stretchable organic optoelectronic sensorimotor synapse. *Sci. Adv.* **4**, eaat7387 (2018).
11. Zhang, J. et al. Spectrum-dependent photonic synapses based on 2d imine polymers for power-efficient neuromorphic computing. *InfoMat* **3**, 904–916 (2021).
12. Choi, S., Yang, J. & Wang, G. Emerging memristive artificial synapses and neurons for energy-efficient neuromorphic computing. *Adv. Mater.* **32**, e2004659 (2020).
13. Zhu, X. & Lu, W. D. Optogenetics-inspired tunable synaptic functions in memristors. *ACS Nano* **12**, 1242–1249 (2018).
14. Zhou, J. et al. A monochloro copper phthalocyanine memristor with high-temperature resilience for electronic synapse applications. *Adv. Mater.* **33**, 2006201 (2020).
15. Gao, S. et al. An oxide Schottky junction artificial optoelectronic synapse. *ACS Nano* **13**, 2634–2642 (2019).
16. Cheng, Z., Rios, C., Pernice, W. H. P., Wright, C. D. & Bhaskaran, H. On-chip photonic synapse. *Sci. Adv.* **3**, e1700160 (2017).
17. Lee, T. H., Loke, D., Huang, K. J., Wang, W. J. & Elliott, S. R. Tailoring transient-amorphous states: Towards fast and power-efficient phase-change memory and neuromorphic computing. *Adv. Mater.* **26**, 7493–7498 (2014).
18. Tuma, T., Pantazi, A., Le Gallo, M., Sebastian, A. & Eleftheriou, E. Stochastic phase-change neurons. *Nat. Nanotechnol.* **11**, 693–700 (2016).
19. Huang, W. et al. Memristive artificial synapses for neuromorphic computing. *Nano-Micro Lett.* **13**, 85 (2021).
20. Wang, Y. et al. Optoelectronic synaptic devices for neuromorphic computing. *Adv. Intell. Syst.* **3**, 2000099 (2020).
21. Zhuge, X., Wang, J. & Zhuge, F. Photonic synapses for ultrahigh-speed neuromorphic computing. *Phys. Status Solidi RRL* **13**, 1900082 (2019).
22. Hao, D. D., Zou, J. & Huang, J. Recent developments in flexible photodetectors based on metal halide perovskite. *InfoMat* **2**, 139–169 (2020).
23. Zhang, J., Dai, S., Zhao, Y., Zhang, J. & Huang, J. Recent progress in photonic synapses for neuromorphic systems. *Adv. Intell. Syst.* **2**, 1900136 (2020).
24. Seo, S. et al. Artificial optic-neural synapse for colored and color-mixed pattern recognition. *Nat. Commun.* **9**, 5106 (2018).
25. Zhou, F. et al. Optoelectronic resistive random access memory for neuromorphic vision sensors. *Nat. Nanotechnol.* **14**, 776–782 (2019).
26. Lou, Z. & Shen, G. Flexible image sensors with semiconducting nanowires for biomimic visual applications. *Small Struct.* **2**, 2000152 (2021).
27. Ham, S., Choi, S., Cho, H., Na, S.-I. & Wang, G. Photonic organolead halide perovskite artificial synapse capable of accelerated learning at low power inspired by dopamine-facilitated synaptic activity. *Adv. Funct. Mater.* **29**, 1806646 (2019).
28. Wang, T. Y. et al. Ultralow power wearable heterosynapse with photoelectric synergistic modulation. *Adv. Sci.* **7**, 1903480 (2020).
29. Yin, L. et al. Synaptic silicon-nanocrystal phototransistors for neuromorphic computing. *Nano Energy* **63**, 103859 (2019).
30. John, R. A. et al. Synergistic gating of electro-iono-photoactive 2d chalcogenide neuristors: Coexistence of Hebbian and homeostatic synaptic metaplasticity. *Adv. Mater.* **30**, 9 (2018).
31. Wang, S. et al. A mos2 /ptcda hybrid heterojunction synapse with efficient photoelectric dual modulation and versatility. *Adv. Mater.* **31**, e1806227 (2019).
32. Wang, H. et al. A ferroelectric/electrochemical modulated organic synapse for ultraflexible, artificial visual-perception system. *Adv. Mater.* **30**, e1803961 (2018).
33. Wei, H. et al. Flexible electro-optical neuromorphic transistors with tunable synaptic plasticity and nociceptive behavior. *Nano Energy* **81**, 105648 (2021).
34. Zhang, J. et al. Tailoring neuroplasticity in flexible perovskite qds-based optoelectronic synaptic transistors by dual modes modulation. *Nano Energy* **95**, 106987 (2022).
35. Yang, Y. et al. Ultraflexible, degradable organic synaptic transistors based on natural polysaccharides for neuromorphic applications. *Adv. Funct. Mater.* **30**, 2006271 (2020).
36. Zhu, H. et al. Wood-derived materials for green electronics, biological devices, and energy applications. *Chem. Rev.* **116**, 9305–9374 (2016).
37. Lei, T. et al. Biocompatible and totally disintegrable semiconducting polymer for ultrathin and ultralightweight transient electronics. *Proc. Natl Acad. Sci. USA* **114**, 5107–5112 (2017).
38. Lu, K. et al. Solution-processed electronics for artificial synapses. *Mater. Horiz.* **8**, 447–470 (2021).
39. Wang, Q. et al. Space-confined strategy toward large-area two-dimensional single crystals of molecular materials. *J. Am. Chem. Soc.* **140**, 5339–5342 (2018).
40. Xu, C. et al. A general method for growing two-dimensional crystals of organic semiconductors by "solution epitaxy". *Angew. Chem., Int. Ed.* **55**, 9519–9523 (2016).
41. Dai, S. et al. Intrinsically ionic conductive cellulose nanopapers applied as all solid dielectrics for low voltage organic transistors. *Nat. Commun.* **9**, 2737 (2018).
42. Liu, Y. H., Zhu, L. Q., Feng, P., Shi, Y. & Wan, Q. Freestanding artificial synapses based on laterally proton-coupled transistors on chitosan membranes. *Adv. Mater.* **27**, 5599–5604 (2015).
43. Lv, Z. et al. Mimicking neuroplasticity in a hybrid biopolymer transistor by dual modes modulation. *Adv. Funct. Mater.* **29**, 1902374 (2019).
44. Wang, Y. et al. Photonic synapses based on inorganic perovskite quantum dots for neuromorphic computing. *Adv. Mater.* **30**, e1802883 (2018).
45. Roe, D. G. et al. Biologically plausible artificial synaptic array: Replicating ebbinghaus' memory curve with selective attention. *Adv. Mater.* **33**, e2007782 (2021).
46. Abbott, L. F. & Regehr, W. G. Synaptic computation. *Nature* **431**, 796–803 (2004).
47. Yin, L. et al. Optically stimulated synaptic devices based on the hybrid structure of silicon nanomembrane and perovskite. *Nano Lett.* **20**, 3378–3387 (2020).

48. Ou, Q. et al. Degradable photonic synaptic transistors based on natural biomaterials and carbon nanotubes. *Small* **17**, e2007241 (2021).
49. Yang, B. et al. Bioinspired multifunctional organic transistors based on natural chlorophyll/organic semiconductors. *Adv. Mater.* **32**, e2001227 (2020).
50. Zhang, J. et al. Retina-inspired organic heterojunction-based optoelectronic synapses for artificial visual systems. *Research* **2021**, 7131895 (2021).
51. Dai, S. et al. Light-stimulated synaptic devices utilizing interfacial effect of organic field-effect transistors. *ACS Appl. Mater. Interfaces* **10**, 21472–21480 (2018).
52. Wang, K. et al. Light-stimulated synaptic transistors fabricated by a facile solution process based on inorganic perovskite quantum dots and organic semiconductors. *Small* **15**, e1900010 (2019).
53. Xu, W., Min, S. Y., Hwang, H. & Lee, T. W. Organic core-sheath nanowire artificial synapses with femtojoule energy consumption. *Sci. Adv.* **2**, e1501326 (2016).
54. Sun, J. et al. Optoelectronic synapse based on igzo-alkylated graphene oxide hybrid structure. *Adv. Funct. Mater.* **28**, 1804397 (2018).

ACKNOWLEDGEMENTS

This work was supported by the National Natural Science Foundation of China (62074111), the Science & Technology Foundation of Shanghai (19JC1412402, 20JC1415600), Shanghai Municipal Science and Technology Major Project (2021SHZDZX0100), Shanghai Municipal Commission of Science and Technology Project (19511132101), and the support of the Fundamental Research Funds for the Central Universities. The authors also thanked the support of Testing & Analysis Center, School of Materials Science and Engineering, Tongji University.

AUTHOR CONTRIBUTIONS

J.Z. with assistance from D.L. and Q.S. conducted the experiments and analyzed the results. B.Y., P.G., L.F., S.D., and L.X. gave suggestions about the experiments. J.Z. and J.H. wrote and revised the paper. J.H. supervised the project.

COMPETING INTERESTS

The authors declare no competing interests.

ADDITIONAL INFORMATION

Supplementary information The online version contains supplementary material available at https://doi.org/10.1038/s41528-022-00163-x.

Correspondence and requests for materials should be addressed to Jia Huang.

Reprints and permission information is available at http://www.nature.com/reprints

Publisher's note Springer Nature remains neutral with regard to jurisdictional claims in published maps and institutional affiliations.